# Delineation of Thermodynamic and Dynamic Responses to Sea Surface Temperature Forcing Associated with El Niño

Xiaoming Hu[1,2], Ming Cai[3], Song Yang[1,2,4] and Zhaohua Wu[3,5]

[1]School of Atmospheric Sciences, Sun Yat-sen University, Guangzhou, China

[2]Guangdong Province Key Laboratory for Climate Change and Natural Disaster Studies, Sun Yat-sen University, Guangzhou, China

[3]Department of Earth, Ocean & Atmospheric Sciences, Florida State University, Tallahassee, Florida, USA

[4]Institute of Earth Climate and Environment System, Sun Yat-sen University, Guangzhou, China

[5]Center for Ocean-Atmospheric Prediction Studies, Florida State University, Tallahassee, USA

Submitted to *Climate Dynamics - EAC Special Issue*

November 2016

**Corresponding author address:* Prof. Song Yang, School of Atmospheric Sciences, Sun Yat-sen University, 135 West Xingang Road, Guangzhou 510275, China. Email: yangsong3@mail.sysu.edu.cn; Prof. Ming Cai, Department of Earth, Ocean & Atmospheric Sciences, Florida State University, Tallahassee, Florida, USA. Email: mcai@fsu.edu

# ABSTRACT

A new framework is proposed to gain a better understanding of the response of the atmosphere over the tropical Pacific to the radiative heating anomaly associated with the sea surface temperature (SST) anomaly in canonical El Niño winters. The new framework is based on the equilibrium balance between thermal radiative cooling anomalies associated with air temperature response to SST anomalies and other thermodynamic and dynamic processes.

The air temperature anomalies in the lower troposphere are mainly in response to radiative heating anomalies associated with SST, atmospheric water vapor, and cloud anomalies that all exhibit similar spatial patterns. As a result, air temperature induced thermal radiative cooling anomalies would balance out most of the radiative heating anomalies in the lower troposphere. The remaining part of the radiative heating anomalies is then taken away by an enhancement (a reduction) of upward energy transport in the central-eastern (western) Pacific basin, a secondary contribution to the air temperature anomalies in the lower troposphere. Above the middle troposphere, radiative effect due to water vapor feedback is weak. Thermal radiative cooling anomalies are mainly in balance with the sum of latent heating anomalies, vertical and horizontal energy transport anomalies associated with atmospheric dynamic response and the radiative heating anomalies due to changes in cloud. The pattern of Gill-type response is attributed mainly to the non-radiative heating anomalies associated with convective and large-scale energy transport. The radiative heating anomalies associated with the anomalies of high clouds also contribute positively to the Gill-type response. This sheds some light on why the Gill-type atmospheric response can be easily identifiable in the upper atmosphere.



**Keywords** El Niño, SST anomalies, thermodynamic and dynamic responses, Gill-type response

## 1. Introduction

The hallmark of an El Niño, in terms of sea surface temperature (SST) anomalies, is the pattern of anomalous warming in the equatorial central-eastern Pacific and cooling in the western equatorial Pacific (Bjerknes 1969; Larkin 2005; Kao and Yu 2009). Associated with the anomalous SST pattern is an eastward shift of the rising branch of the Walker Circulation from the equatorial western Pacific to the central Pacific. The eastward shifting of the Walker Circulation is manifested by upward (downward) motion anomalies and anomalous divergence (convergence) in the upper troposphere over the central equatorial (western) Pacific region (Zebiak 1986; Trenberth et al. 1998; Ashok et al. 2007; Yuan and Yang 2012). Associated with the anomalous divergence flow is a pair of off-equator anti-cyclonic circulation anomalies on the west and an equatorial positive center of geopotential height anomaly on the east (Gill 1980; Rasmusson and Kingtse Mo 1993). For an easy reference, we refer to such spatial pattern of geopotential height anomaly as a positive "tripod" of circulation anomalies. The off-equator anti-cyclonic circulation anomalies serve as the source of Rossby wave train emanating from deep tropic into the extratropics along the great circle route (Hoskins and Karoly 1981; Philander 1990; Trenberth et al. 1998). In this way, an El Niño leads to profound impacts on weather and climate over the globe, including remote regions via teleconnections (Wang et al. 2000; Alexander et al. 2002; Lyon and Barnston 2005; Ashok et al. 2007; Wang et al. 2012). Besides this positive tripod, there exists a negative tripod associated with the downward motion anomalies over the western equatorial Pacific, namely a pair of off-equator anomalous cyclonic centers on the west and a negative geopotential height center on the east centered at around l50° E (DeWeaver and Nigam 2004).

Gill (1980) provided an analytic solution of the idealized atmospheric dynamic response to a localized diabatic heating anomaly center, which exhibits a positive tripod spatial pattern. It

74 represents the dynamic balance of a pair of westward propagating Rossby anti-cyclonic circulation
75 anomalies and an eastward propagating high-pressure Kelvin mode in the upper troposphere with
76 the positive diabatic heating anomalies below. Conversely, a negative tripod spatial pattern in the
77 upper troposphere can be regarded as the Gill-type response to a diabatic cooling anomaly.
78 DeWeaver and Nigam (2004) used a linear general circulation model to prove that, in the upper
79 troposphere during the mature phase of El Niño events, the co-existence of a positive tripod of
80 circulation anomalies over the central tropical Pacific and a negative tripod above the western
81 tropical Pacific can be regarded as the Gill-type response to a pair of localized heating anomalies
82 of opposite sign with positive in the east and negative in the west.

83 The Gill solution also predicts that there is a tripod with the opposite sign in the lower
84 troposphere centered at the localized diabatic heating center (Wu et al. 2000; Wu 2003). In other
85 words, one would expect a negative (positive) tripod spatial pattern over the tropical (western)
86 Pacific in the lower troposphere during El Niño events, if the Gill-type response would prevail.
87 However, during El Niño events, geopotential height anomalies in the lower troposphere do exhibit
88 negative values over the tropical eastern Pacific but positive values over the western equatorial
89 Pacific, indicating a negative Southern Oscillation pattern (Rasmusson and Carpenter 1982;
90 Rasmusson and Wallace 1983). The accompanied off-equator circulation anomalies of the same
91 sign as in the Gill-type response are not identifiable in the lower troposphere. The lack of Gill-type
92 dynamic response signal in the lower atmosphere seems to indicate that the thermodynamic
93 response would have to play a more important role in the observed response to SST anomalies in
94 the lower troposphere. Thermodynamic processes yield different spatial patterns in the lower-
95 tropospheric response to SST anomalies of El Niño events, especially near the surface (Lindzen
96 and Nigam 1987; Battisti et al. 1999; Chiang et al. 2001; Back and Bretherton 2009). Battisti et al.

97 (1999) found that the circulation anomalies near the surface were forced by sensible and latent
98 heat flux anomalies while circulation anomalies above the boundary layer were forced by the latent
99 heating anomaly. Furthermore, Chiang et al. (2001) reported that the Gill type response above the
100 boundary layer contributed significantly to the surface zonal wind but the meridional wind was
101 primarily forced by the gradient of SST anomalies associated with El Niño events. Back and
102 Bretherton (2009) and Zhang et al. (2012) discussed the relative contributions from the
103 thermodynamic process in the boundary layer and the dynamic process above the boundary layer.
104 The existence of clearly organized Gill-type response in the middle and upper troposphere but less
105 organized one in the lower troposphere had been duplicated in model simulations of El Niño (Lee
106 et al. 2009).

107 The main objective of this study is to delineate the roles of the thermodynamic and dynamic
108 responses to SST anomalies associated with canonical El Niño events. Because geopotential height
109 and air temperature anomalies are related to one another via the hydrostatic balance (White 2008),
110 we will focus on air temperature response in this study. Specifically, we wish to examine how the
111 response in atmospheric temperature transitions from the thermodynamically-driven response in
112 the lower troposphere, which resembles to the SST anomaly pattern, to the pattern characterized
113 by the Gill-type response in the upper atmosphere. The remaining part of this paper is organized
114 as follows. Section 2 presents the analysis framework of the coupled dynamic and thermodynamic
115 responses and Section 3 describes data and analysis procedures. Features of atmospheric response
116 to SST anomalies associated with El Niño events are presented in Section 4. Section 5 discusses

117 the attribution of temperature response to individual radiative and non-radiative heating anomalies.
118 Conclusions are given in Section 6.

119 ## 2. Analysis Framework

120 A new framework is proposed to delineate the atmosphere response to SST anomalies. The
121 main feature of this new framework is to divide loosely the atmosphere response to anomalous
122 upward longwave radiative fluxes associated with SST anomalies into two parts: non-temperature
123 response and temperature response. Non-temperature response includes the changes in
124 atmospheric dynamics processes, such as those in convective activity and large-scale atmospheric
125 circulation (e.g., the Gill-type response), as well as the changes in non-temperature thermodynamic
126 variables such as water vapor and cloud anomalies. The changes in atmospheric dynamics
127 processes redistribute energy both vertically and horizontally far away from the original diabatic
128 heating anomaly, but also generate additional heating anomalies, such as latent heat anomalies.
129 Associated with the changes in non-temperature thermodynamic variables are radiative heating
130 anomalies. It is the anomaly of thermal radiative cooling rate associated with the changes in air
131 temperatures that is in balance with the sum of these individual non-temperature induced radiative
132 heating anomalies and non-radiative energy flux convergence anomalies.

133 The formulation of the new framework is based on the perturbation equation of energy
134 balance in an atmospheric column from the boundary layer to the top layer, namely,

135 $$\Delta^{(RAD)}Q + \Delta^{(DYN)}Q = 0 \quad \Delta^{(RAD)}Q + \Delta^{(DYN)}Q = 0 \qquad (1)$$

136 where $\Delta^{(RAD)}Q$ $\Delta^{(RAD)}Q$ corresponds to the vertical profile of total changes in radiative energy
137 absorbed by the atmosphere. $\Delta^{(DYN)}Q$ $\Delta^{(DYN)}Q$ corresponding to the vertical profile of non-

Field Code Changed

Field Code Changed

Field Code Changed

radiative energy flux convergence anomalies, which are equal to the sum of perturbations in energy redistributions by convective and large-scale atmospheric motions as well as changes in energy fluxes entering the atmosphere due to the changes in surface sensible and latent heat fluxes. By evoking a linear approximation, we have

~~$\Delta^{(RAD)}Q \approx \Delta Q^{(T_s)} + \Delta^{(WV)}Q + \Delta^{(C)}Q - \Delta^{(T_{air})}R + \Delta^{(other)}Q$~~

$$\Delta^{(RAD)}Q \approx \Delta^{(T_S)}Q + \Delta^{(WV)}Q + \Delta^{(C)}Q - \Delta^{(T_{air})}R + \Delta^{(other)}Q \quad (2)$$

where $\Delta^{(T_S)}Q$ ~~$\Delta^{(T_s)}Q$~~ is the vertical profile of the absorption of the perturbation longwave radiative flux emitted from the surface associated with SST anomalies. $\Delta^{(WV)}Q$ ~~$\Delta^{(WV)}Q$~~ and $\Delta^{(C)}Q$ ~~$\Delta^{(C)}Q$~~ are the vertical profiles of the absorption perturbation of the shortwave and longwave radiative energy due to the changes in atmospheric water vapor (WV) and clouds (C), respectively. $\Delta^{(T_{air})}R$ ~~$\Delta^{(T_{air})}R$~~ is the vertical profile of radiative thermal cooling rate anomalies due to atmospheric temperature ($T_{air}$) anomalies, and $\Delta^{(other)}Q$ denotes the vertical profile of the absorption perturbation of radiative energy fluxes due to the changes in stratospheric ozone and surface albedo. Because the part of $\Delta^{(other)}Q$ ~~$\Delta^{(other)}Q$~~ due to the change in ozone is very small in the troposphere and the part of $\Delta^{(other)}Q$ ~~$\Delta^{(other)}Q$~~ due to the change in surface albedo is nearly equal to zero over tropical oceans,

Field Code Changed
Field Code Changed
Field Code Changed
Field Code Changed
Field Code Changed
Field Code Changed
Field Code Changed

we neglect the term $\Delta^{(other)}Q$ ~~$\Delta^{(other)}Q$~~ in this study. Combining (1) and (2) without the term $\Delta^{(other)}Q$ ~~$\Delta^{(other)}Q$~~ yields

$$\Delta^{(T_{air})}R \approx \Delta^{(T_S)}Q + \Delta^{(WV)}Q + \Delta^{(C)}Q + \Delta^{(DYN)}Q \quad (3)$$

Next, we calculate the pattern-amplitude projection (PAP; Deng et al. 2012) coefficients according to

$$PAP_j^{(X)} = \frac{A^{-1}\int_A a^2 \Delta^{(X)}Q_j \Delta^{(T_{air})}R_j \cos\phi d\lambda d\phi}{\sqrt{A^{-1}\int_A a^2 (\Delta^{(T_{air})}R_j)^2 \cos\phi d\lambda d\phi}} \quad PAP_j^{(X)} = \frac{A^{-1}\int_A a^2 \Delta^{(X)}Q_j \Delta^{(T_{air})}Q_j \cos\phi d\lambda d\phi}{\sqrt{A^{-1}\int_A a^2 (\Delta^{(T_{air})}Q_j)^2 \cos\phi d\lambda d\phi}} \quad (4)$$

where $\phi$ and $\lambda$ are respectively latitude and longitude, and $a$ is the radius of the earth. A corresponds to the area of the tropical Pacific domain of 30 °S-30 °N, 90 °E-90 °W. $\Delta^{(X)}Q_j$ ~~$\Delta^{(X)}Q_j$~~ is one of the terms on the right hand side (RHS) of (3) in the j$^{th}$ atmospheric layer. It is easy to verify that according (3) the summation of $PAP_j^{(X)}$ ~~$PAP_j^{(X)}$~~ over all terms on the RHS of (3) is approximately equal to the amplitude of the spatial pattern of $\Delta^{(T_{air})}R_j$ ~~$\Delta^{(T_{air})}Q_j$~~ over the area A, namely, $\sum_X PAP_j^{(X)} \approx \sqrt{A^{-1}\int_A a^2 (\Delta^{(T_{air})}R_j)^2 \cos\phi d\lambda d\phi}$

~~$\sum_X PAP_j^{(X)} \approx \sqrt{A^{-1}\int_A a^2 (\Delta^{(T_{air})}Q_j)^2 \cos\phi d\lambda d\phi}$~~ (the approximation is due to the linearization of the radiative transfer model and the neglecting of the small term $\Delta^{(other)}Q$ ~~$\Delta^{(other)}Q$~~). Therefore, $PAP_j^{(X)}$ ~~$PAP_j^{(X)}$~~ measures the relative contribution of each term on the RHS of (3) to $\Delta^{(T_{air})}R$ ~~$\Delta^{(T_{air})}R$~~ in the j$^{th}$ atmospheric layer in terms of both spatial pattern and amplitude. It follows that

Field Code Changed
Field Code Changed
Field Code Changed
Field Code Changed
Field Code Changed
Field Code Changed
Field Code Changed
Field Code Changed
Field Code Changed
Field Code Changed
Field Code Changed

the closer the value of $PAP_j^{(X)}$ ~~$PAP_j^{(X)}$~~ to the amplitude of the spatial pattern of $\Delta^{(T_{air})}R_j$ ~~$\Delta^{(T_{air})}Q_j$~~, the larger is contribution of the corresponding process to both spatial pattern and amplitude of temperature response. Thus, we can say that the atmospheric temperature change in the layer over area A is mainly in response to the process X because the radiative cooling associated with air temperature change ($\Delta^{(T_{air})}R_j$ ~~$\Delta^{(T_{air})}Q_j$~~) is mainly in balance with $\Delta^{(X)}Q_j$ ~~$\Delta^{(X)}Q_j$~~.

Field Code Changed

Field Code Changed

Field Code Changed

Field Code Changed

## 3. Data and Analysis Procedures

The data used in this study are obtained from the European Centre for Medium-range Weather Forecasts (ECMWF) Re-Analysis Interim (ERA-Interim; Dee and Uppala 2009; Dee et al. 2011). The atmospheric variables include geopotential height, air temperature, specific humidity, ozone mixing ratio, cloud cover, and cloud liquid/ice water content. All atmospheric variables are defined at 37 pressure levels from 1000 hPa to 1 hPa. We also consider the incoming solar energy flux at the top of the atmosphere (TOA), the surface skin temperature, the upward longwave radiative flux at the surface, surface albedo, and surface sensible/latent heat fluxes.

Following Hu et al. (2016), we use the data in the periods of the four major canonical El Niño winters (1982/1983, 1986/1987, 1997/1998, and 2006/2007) and eight ENSO-neutral winters (1980/1981, 1981/1982, 1985/1986, 1989/1990, 1992/1993, 1993/1994, 2001/2002, and 2003/2004) to construct the composite El Niño and neutral events, respectively. The differences (denoted by the symbol Δ) between the composite El Niño and neutral events are referred to as El

187 Niño anomalies. We focus on the El Niño anomalies over the tropical Pacific and part of the East
188 Asia monsoon region (30 °S-30 °N, 80 °E-80 °W).

189 We use the Fu-Liou radiative transfer model (Fu and Liou 1992; Fu and Liou 1993) to evaluate
190 all terms in (2) at the original 37 levels of the ERA-interim on each grid point as the following:

191
$$\Delta^{(RAD)}Q = Q(T_{SST}^{E}, T_{air}^{E}, WV_{air}^{E}, C_{air}^{E}, other_{air}^{E}) - Q(T_{SST}^{N}, T_{air}^{N}, WV_{air}^{N}, C_{air}^{N}, other_{air}^{N})$$

$$\Delta Q^{(T_s)} = Q(T_{SST}^{E}, T_{air}^{N}, WV_{air}^{N}, C_{air}^{N}, other_{air}^{N}) - Q(T_{SST}^{N}, T_{air}^{N}, WV_{air}^{N}, C_{air}^{N}, other_{air}^{N})$$

$$\Delta^{(WV)}Q = Q(T_{SST}^{N}, T_{air}^{N}, WV_{air}^{E}, C_{air}^{N}, other_{air}^{N}) - Q(T_{SST}^{N}, T_{air}^{N}, WV_{air}^{N}, C_{air}^{N}, other_{air}^{N})$$

$$\Delta^{(C)}Q = Q(T_{SST}^{N}, T_{air}^{N}, WV_{air}^{N}, C_{air}^{E}, other_{air}^{N}) - Q(T_{SST}^{N}, T_{air}^{N}, WV_{air}^{N}, C_{air}^{N}, other_{air}^{N})$$

$$\Delta^{(T_{air})}R = -[Q(T_{SST}^{N}, T_{air}^{E}, WV_{air}^{N}, C_{air}^{N}, other_{air}^{N}) - Q(T_{SST}^{N}, T_{air}^{N}, WV_{air}^{N}, C_{air}^{N}, other_{air}^{N})]$$

$$\Delta^{(other)}Q = Q(T_{SST}^{N}, T_{air}^{N}, WV_{air}^{N}, C_{air}^{N}, other_{air}^{E}) - Q(T_{SST}^{N}, T_{air}^{N}, WV_{air}^{N}, C_{air}^{N}, other_{air}^{N})$$

192
$$\begin{aligned}
&\Delta^{(RAD)}Q = Q(T_{SST}^{E}, T_{air}^{E}, WV_{air}^{E}, C_{air}^{E}, other_{air}^{E}) - Q(T_{SST}^{N}, T_{air}^{N}, WV_{air}^{N}, C_{air}^{N}, other_{air}^{N}) \\
&\Delta^{(T_S)}Q = Q(T_{SST}^{E}, T_{air}^{N}, WV_{air}^{N}, C_{air}^{N}, other_{air}^{N}) - Q(T_{SST}^{N}, T_{air}^{N}, WV_{air}^{N}, C_{air}^{N}, other_{air}^{N}) \\
&\Delta^{(WV)}Q = Q(T_{SST}^{N}, T_{air}^{N}, WV_{air}^{E}, C_{air}^{N}, other_{air}^{N}) - Q(T_{SST}^{N}, T_{air}^{N}, WV_{air}^{N}, C_{air}^{N}, other_{air}^{N}) \\
&\Delta^{(C)}Q = Q(T_{SST}^{N}, T_{air}^{N}, WV_{air}^{N}, C_{air}^{E}, other_{air}^{N}) - Q(T_{SST}^{N}, T_{air}^{N}, WV_{air}^{N}, C_{air}^{N}, other_{air}^{N}) \\
&\Delta^{(T_{air})}R = -\left[Q(T_{SST}^{N}, T_{air}^{E}, WV_{air}^{N}, C_{air}^{N}, other_{air}^{N}) - Q(T_{SST}^{N}, T_{air}^{N}, WV_{air}^{N}, C_{air}^{N}, other_{air}^{N})\right] \\
&\Delta^{(other)}Q = Q(T_{SST}^{N}, T_{air}^{N}, WV_{air}^{N}, C_{air}^{N}, other_{air}^{E}) - Q(T_{SST}^{N}, T_{air}^{N}, WV_{air}^{N}, C_{air}^{N}, other_{air}^{N})
\end{aligned} \quad (5)$$

Field Code Changed

193 where Q is the vertical profile of the net radiative energy flux convergence (in units of $W/m^2$) in
194 each atmospheric layer obtained from the radiative transfer model using the information of SST,
195 vertical profiles of $T_{air}$, WV, and C, as well as other variables/parameters (denoted as "other") such
196 as the incoming solar radiative flux at the TOA, ozone, and surface albedo. The superscript "N"
197 and "E" denote, respectively, the variables derived from the composite mean fields of the eight

ENSO-neutral winters and the four major El Niño winters. Note that the vertical profiles of C include cloud liquid and ice water as well as cloud area. We then use (1) to indirectly infer the term $\Delta^{(DYN)}Q$ ~~$\Delta^{(DYN)}Q$~~ as

$$\Delta^{(DYN)}Q = -\Delta^{(RAD)}Q \quad \text{or} \quad \Delta^{(DYN)}Q = -\Delta^{(RAD)}Q \tag{6}$$

Equations (5) and (6) enable us to obtain all of the terms in (3).

Note that because the units of all terms in (5) have been converted from K/s (degree per second) to W/m$^2$, they can be summed up vertically without changing their physical meanings. For example, the vertical summation of $\Delta^{(WV)}Q$ ~~$\Delta^{(WV)}Q$~~ from the lowest to the highest atmospheric layers corresponds to the perturbation in the total energy absorbed by the atmosphere due to the changes in atmospheric water vapor. Therefore, we can reduce the number of layers in our discussions to a few selected layers by adding the terms vertically. We have divided the atmospheric column broadly into six layers in presenting the results of (3) and (4): one for the boundary layer (1000-925 hPa), two for the lower troposphere (925-800 hPa and 800-600 hPa), one for the middle troposphere (600-400 hPa), and two for the upper troposphere (400-250 hPa and 250-150 hPa). We will use the results in these layers to the explain temperature and geopotential height anomalies at 950 hPa, 850 hPa, 700 hPa, 500 hPa, 300 hPa, and 200 hPa.

Field Code Changed

Field Code Changed

Field Code Changed

## 4. An Overview of the Key Features of Atmospheric Anomalies of El Niño Events

We here present an overview of the salient features of atmospheric circulation anomalies observed during El Niño events. Figure 1a shows the composite SST anomalies over the tropical Pacific during El Niño winters. The corresponding geopotential height anomalies at various levels are displayed in Fig. 2. It is seen that in the upper troposphere above 500 hPa, there exists a pair

of negative and positive tripods of circulation anomalies centered over the western and eastern tropical Pacific, respectively (Figs. 2a-b). The intensity of geopotential height anomalies is strongest at 200 hPa. The existence of such a pair of tripods in the upper troposphere is consistent with the Gill-type response to a pair of localized heating anomalies of opposite sign with positive values in the east and cooling anomalies in the west (DeWeaver and Nigam 2004). Below the middle troposphere (Figs. 2d-f), the geopotential height response mainly shows negative values over the tropical eastern Pacific but positive values over the western Pacific, indicating the negative Southern Oscillation pattern during El Niño winters (Rasmusson and Wallace 1983; Scherllin-Pirscher et al. 2011). The off-equator positive and negative centers are barely noticeable. Therefore, the canonical low-level Gill-type response is not observed in the lower troposphere. The lack of Gill-type dynamic response signal in the lower atmosphere seems to indicate that the thermodynamic response could play a more important role in the observed response to SST anomalies in the lower troposphere.

It is seen from Fig. 3 that the spatial pattern of air temperature anomalies in the lower troposphere is similar to SST anomalies. The Gill-type response begins to emerge clearly at 500 hPa with the maximum intensity at 300 hPa. Therefore, one would infer from the hydrostatic balance that the pair of tripod patterns in geopotential height anomalies exists only at levels higher 500 hPa with its intensity increasing with elevation until a level above 300 hPa. According to Fig. 2, the maximum amplitude of the tripod patterns in the field of geopotential height anomaly is at 200 hPa. The ability of using the hydrostatic balance to infer geopotential height anomalies from air temperature response to SST anomalies is the rationale that prompts us to focus on air temperature response in the framework of (3) for explaining the dominance of the

thermodynamically-driven response in the lower troposphere but the Gill-type response in the upper troposphere.

Now let us examine the anomaly fields that are responsible for the energy flux convergence perturbations on the RHS of (3). The anomalous upward longwave radiative flux emitted from the surface during El Niño events ( $\Delta R_S^{\uparrow}$ ~~$\Delta R_s^{\uparrow}$~~, Fig. 1b) can be inferred directly from the corresponding SST anomalies (Fig. 1a) using $\Delta R_s^{\uparrow} \approx 4\sigma \overline{T}_s^3 \Delta T_s$ ~~$\Delta R_s^{\uparrow} \approx 4\sigma \overline{T}_s^3 \Delta T_s$~~ ,where σ is the Stefan-Boltzmann constant and $\overline{T}_s^3$ ~~$\overline{T}_s$~~ is the mean SST derived from the composite mean of neutral events. The term $\Delta R_S^{\uparrow}$ ~~$\Delta R_s^{\uparrow}$~~ can be regarded as the "source of external forcing" for the atmospheric response since its absorption by the atmosphere, i.e. the first term on the RHS of (3), is the "sole" source of energy outside the atmosphere component of the coupled atmosphere-ocean system in the analysis framework (3). Here we wish to reiterate that the anomalous surface latent and sensible fluxes should also be regarded as part of the "external forcing" to the atmosphere component. However, the effect of anomalous surface latent and sensible fluxes entering the atmosphere has been blended in the last term on the RHS of (3) as part of the atmospheric dynamic response since there is no information available from the ERA-interim about where the energy is released without running a general circulation model.

Field Code Changed

Field Code Changed

Field Code Changed

Field Code Changed

The atmospheric water vapor anomalies of the composite El Niño (Fig. 4) exhibit a similar spatial pattern as the SST anomalies, showing a moistening center in the central-eastern equatorial Pacific and drying anomalies in the western equatorial Pacific and off-equator tropical latitudes in both hemispheres, which is consistent with the results Prabhakara et al. (1985) and Takahashi et al. (2013). The horizontal pattern of atmospheric water vapor anomalies remains largely

unchanged throughout the troposphere but its amplitude decreases gradually with height in the lower troposphere and diminishes in the upper troposphere. The cloud water/ice content anomalies of the composite El Niño, however, exhibit large amplitude in the middle and upper troposphere (Figs. 5b-5d). The spatial pattern of cloud water/ice content anomalies in the middle and upper troposphere resembles greatly to that of the rainfall anomalies of the composite El Niño (Fig. 6), suggesting that most of condensation or latent heating anomaly takes place in the middle and upper troposphere. This conjecture is consistent with the vertical motion anomalies of the composite El Niño (Fig. 7). Specifically, the spatial patterns of vertical motion anomalies at 700 hPa, 500 hPa, and 300 hPa (Figs. 7b-7d) are all similar not only to one another but also to the cloud water/ice content anomalies at these layers (Figs. 5b-5d) and rainfall anomalies (Fig. 6). The nearly perfect positive correlation among these spatial patterns indicates that the most latent heating anomalies take place in the layers between 700 hPa and 300 hPa where both vertical motion and cloud content anomalies are strongest and their spatial patterns match the spatial pattern of rainfall anomalies. The pattern of downward motion anomalies with less clouds and reduction of rainfall over the western equatorial Pacific and upward motion anomalies with more clouds and enhancement of rainfall over the central-eastern Pacific is indicative of the weakening of the Walker Circulation during the mature phase of El Niño (Philander 1990; Hsu 1994; Power and Smith 2007). The dominance of the downward motion anomalies away from the equator, together with the dominance of the rising motion anomalies along the equatorial Pacific, is suggestive of the strengthening of the Hadley Circulation (Oort and Yienger 1996; Sun et al. 2013; Nguyen et al. 2013).

In summary, the key features of the non-air temperature changes along the equatorial Pacific associated with the SST anomalies of the composite El Niño are (i) strengthening (weakening) of

the upward thermal radiative fluxes emitted from the ocean surface in the central-eastern (western) equatorial Pacific, (ii) moistening (drying) in the lower troposphere along the central-eastern (western) equatorial Pacific, and (iii) more (less) latent heating release accompanied with more (less) clouds in the middle and upper troposphere along the central-eastern (western) equatorial Pacific. In the next section, we will consider the effects of radiative heating and non-radiative energy flux anomalies and examine how they are balanced by radiative thermal cooling anomalies associated with air temperature response.

## 5. Attribution of Air Temperature Response to Anomalies of Radiative and Non-radiative Processes

The anomalies of the radiative thermal cooling rate associated with the air temperature anomalies at the 6 layers of 950 hPa, 850 hPa, 700 hPa, 500 hPa, 300 hPa, and 200 hPa (Fig. 8) exhibit similar spatial patterns as the air temperature anomalies shown in Fig. 3, which is expected because warm (cold) air temperature anomalies would emit more (less) thermal energy. We now attribute the air temperature anomalies to radiative and non-radiative heating rate perturbations by examining their balance with the air temperature induced radiative heating anomalies during El Niño winters. Figure 9 shows the pattern-amplitude projection coefficients of each term on the RHS of (3) onto the left hand side (i.e., $\Delta^{(T_{air})}R$ $\Delta^{(T_{air})}R$ shown in Fig. 8) as a function of height.

Field Code Changed

It is seen from Fig. 9 that the response to SST anomalies accounts for nearly 80% of the spatial pattern of the air temperature induced anomalies of radiative thermal cooling rate ($\Delta^{(T_{air})}R$ $\Delta^{(T_{air})}R$) in the boundary layer (1000-925 hPa). Most of energy emitted from the surface due to SST anomalies (Fig. 1b) is absorbed in the boundary layer (Fig. 10f), explaining why the air temperature response in the boundary layer resembles to the SST anomalies greatly. Above the boundary layer,

Field Code Changed

307 the direct effect of SST anomalies diminishes very quickly (Figs. 10a-10e). Because SST
308 anomalies no longer play a direct role in causing air temperature change above the boundary layer,
309 the spatial pattern of air temperature anomalies differs from the SST anomaly pattern more and the
310 difference increases as elevation goes up (see the orange portion of the bars in Fig. 9).

311 Displayed in Fig. 11 are the radiative heating rate anomalies due to the change in atmospheric
312 water vapor ($\Delta^{(WV)}Q$ ~~$\Delta^{(WV)}Q$~~). As discussed in Sejas et al. (2016), an increase of atmospheric
313 greenhouse gases in a tropospheric layer, such as atmospheric water vapor, would lead to large
314 positive (weak negative) radiative heating anomalies in the layers below (above). The reversal can
315 be said for a decrease of atmospheric water vapor in a tropospheric layer. Recall that atmospheric
316 water anomalies (Fig. 4) tend to concentrate below the middle troposphere and are positively
317 correlated with SST anomalies. This feature explains why the spatial pattern of $\Delta^{(WV)}Q$ ~~$\Delta^{(WV)}Q$~~ in
318 the lower troposphere (panels (d)-(f) of Fig. 11) is positively correlated with SST anomalies but
319 negatively correlated with $\Delta^{(WV)}Q$ ~~$\Delta^{(WV)}Q$~~ in the upper troposphere (panels (a)-(c) of Fig. 11). As
320 a result, $\Delta^{(WV)}Q$ ~~$\Delta^{(WV)}Q$~~ contributes to the air temperature changes positively and strongly in the
321 lower troposphere but negatively and weakly in the upper troposphere (see the green portion of
322 the bars in Fig. 9).

323 We have confirmed that different from the surface, throughout the atmosphere the longwave
324 portion of the radiative heating rate anomalies ($\Delta^{(C)}Q$ ~~$\Delta^{(C)}Q$~~) or the greenhouse effect is greater
325 than the shortwave portion or the reflection effect (Bergman and Hendon 2000; Wang and Su
326 2013). Therefore, the behavior of the net effect of $\Delta^{(C)}Q$ ~~$\Delta^{(C)}Q$~~ is similar to the effect of $\Delta^{(WV)}Q$
327 ~~$\Delta^{(WV)}Q$~~, as far as the sign is concerned, namely large positive (weak negative) radiative heating

Field Code Changed
Field Code Changed
Field Code Changed
Field Code Changed
Field Code Changed
Field Code Changed

anomalies below (above) the layer where cloud content anomalies are positive. Unlike atmospheric water vapor, which mainly resides in the lower troposphere, clouds and their changes can take place largely in the upper troposphere. This is especially true for the equatorial region where cloud anomalies are associated with the changes in deep convection as both cloud and upward motion anomalies are large and are positively correlated one another even in the upper troposphere (Fig. 5 versus Fig. 7). In light of the aforementioned factors, one would expect positive values of $\Delta^{(C)}Q$ ~~$\Delta^{(C)}Q$~~ over the central-eastern equatorial Pacific throughout the troposphere but negative values over the western equatorial Pacific (Fig. 12) due to the weakening of the Walker Circulation or the weakening (strengthening) of deep convections over the western (central-eastern) equatorial Pacific. As a result, $\Delta^{(C)}Q$ ~~$\Delta^{(C)}Q$~~ contributes positively to the air temperature changes along the equatorial Pacific throughout the troposphere. In the lower troposphere, $\Delta^{(C)}Q$ ~~$\Delta^{(C)}Q$~~ also contributes positively to the air temperature anomalies outside the equatorial basin, becoming the leading contributor to $\Delta^{(C)}Q$ ~~$\Delta^{(C)}Q$~~ over the entire tropical Pacific in the layer of 925-800 hPa (gray portion of the bars in Fig. 9). In the upper troposphere, $\Delta^{(C)}Q$ ~~$\Delta^{(C)}Q$~~ is weakly correlated with $\Delta^{(T_{air})}R$ ~~$\Delta^{(T_{air})}R$~~ outside the equatorial basin, partially because the amplitude of cloud anomalies becomes weaker away from the equatorial latitude band in the upper troposphere. As a result, the positive contribution from $\Delta^{(C)}Q$ ~~$\Delta^{(C)}Q$~~ to $\Delta^{(T_{air})}R$ ~~$\Delta^{(T_{air})}R$~~ becomes secondary in the upper troposphere.

The non-radiative heating anomalies ($\Delta^{(DYN)}Q$ ~~$\Delta^{(DYN)}Q$~~) include latent heat release anomalies and perturbations in energy redistributions by convective and large-scale atmospheric motions as well as changes in energy fluxes entering the atmosphere due to the changes in surface sensible

Field Code Changed
Field Code Changed
Field Code Changed
Field Code Changed
Field Code Changed
Field Code Changed
Field Code Changed
Field Code Changed

and latent heat fluxes. Overall, the non-radiative heating anomalies are negatively correlated with the upward motion (−ω) anomalies (i.e., Fig. 13 versus Fig. 7), particularly along the equatorial latitude band. This seems to indicate that the non-radiative heating anomalies are mainly associated with the energy redistributions by convective and large-scale atmospheric motions because latent heat release anomalies are expected to be positively correlated with upward motion anomalies. In other words, the negative (positive) values of $\Delta^{(DYN)}Q$ ~~$\Delta^{(DYN)}Q$~~ in Fig. 13 are indicative of divergence (convergence) of energy transport by convection and/or large-scale dynamics. The longitudinal pattern of $\Delta^{(DYN)}Q$ ~~$\Delta^{(DYN)}Q$~~ along the equatorial Pacific basin suggests an enhancement (reduction) of upward energy transport associated with the convection in the central (western) Pacific and reduction of energy transport from the western equatorial Pacific to central-eastern equatorial Pacific. Each of these two possible scenarios is a direct evidence of the weakening of the Walker Circulation during El Niño. The meridional pattern of $\Delta^{(DYN)}Q$ ~~$\Delta^{(DYN)}Q$~~ is indicative of strengthening (weakening) of poleward energy transport over the central-eastern (western) tropical Pacific sector. Overall, $\Delta^{(DYN)}Q$ ~~$\Delta^{(DYN)}Q$~~ contributes to air temperature changes positively in the middle and upper troposphere but negatively in the lower troposphere (the blue portion of the bars in Fig. 9). In particular, $\Delta^{(DYN)}Q$ ~~$\Delta^{(DYN)}Q$~~ becomes the leading contributor to $\Delta^{(T_{air})}R$ ~~$\Delta^{(T_{air})}R$~~ at 200 hPa.

Field Code Changed

Field Code Changed

Field Code Changed

Field Code Changed

Field Code Changed

Field Code Changed

## 6. Conclusions

Using the ERA-Interim reanalysis data set, four major canonical El Niño events and eight neutral cases are selected for the period of 1979-2013. The DJF-mean differences between the two groups are regarded as the composite anomalies for the mature phase of the canonical El Niño. We

have confirmed that the spatial pattern of air temperature anomalies in the lower troposphere is similar to SST anomaly pattern and the Gill-type response begins to emerge mainly in the layers above 500 hPa with the maximum intensity at 300 hPa. To gain a better understanding of why the Gill-type response to SST anomalies over the tropical Pacific during El Niño mature phase is observed mainly in the upper troposphere, we examine the balance of thermal radiative cooling anomalies associated with air temperature response to SST anomalies with other thermodynamic and dynamic processes.

Most of the anomalous upward longwave radiative fluxes associated SST anomalies are absorbed in the boundary layer. In response to such heating anomalies, air temperature anomalies in the boundary layer exhibit a similar spatial pattern as the SST anomalies so the associated thermal radiative cooling anomalies would balance out most of the absorbed energy. The moistening and more clouds in the lower troposphere produce positive radiative heating anomalies in the central-eastern equatorial Pacific but drying and less clouds in the western equatorial Pacific introduce negative radiative heating anomalies. The air temperature anomalies in the lower troposphere are mainly in response to water vapor and cloud-induced radiative heating anomalies to reach a radiative equilibrium balance. The remaining part of the radiative heating anomalies is taken away by an enhancement (a reduction) of upward energy transport in the central-eastern (western) Pacific basin. The non-radiative heating anomalies associated with the changes in dynamics contribute secondarily to the air temperature anomalies in the lower troposphere. The dominance of the thermodynamic response in the lower troposphere explains why the Gill-type

response in the low levels is identifiable mainly in a dynamic model that does not include radiative heating processes.

Above the middle troposphere, the radiative effect due to water vapor feedback is weak. Thermal radiative cooling anomalies are mainly in balance with the sum of latent heating anomalies, the vertical and horizontal energy transport anomalies associated with atmospheric dynamic response, and the radiative heating anomalies due to cloud changes. The pattern of Gill-type response is attributed mainly to non-radiative heating anomalies associated with convective and large-scale energy transport. The radiative heating anomalies associated with the anomalies of high clouds also contribute positively to the Gill-type response. This feature sheds light on why the Gill-type atmospheric response can be easily identifiable in the upper atmosphere.

**Acknowledgement**

This study was supported by The National Key Research and Development Program of China (2016YFA0602703), the National Key Research Program of China (2014CB953904), the National Natural Science Foundation of China (Grants 41661144019 and 41375081), and the Jiangsu Collaborative Innovation Center for Climate Change, China. MC is supported by grants from the National Science Foundation (AGS-1354834) and NASA Interdisciplinary Studies Program grant (NNH12ZDA001N-IDS). Calculations for this study were supported by the High-Performance Grid Computing Platform of the Sun Yat-sen University and the China National Supercomputer Center in Guangzhou. The data sets used in this study are all freely available on the official websites of http://apps.ecmwf.int/datasets/data/interim-full-mnth/.

411 **References**


412 Alexander MA, Bladé I, Newman M, et al (2002) The atmospheric bridge: the influence of
413 ENSO teleconnections on air–sea interaction over the global oceans. J Climate 15: 2205–
414 2231. doi: 10.1175/1520-0442(2002)015<2205:TABTIO>2.0.CO;2

415 Ashok K, Behera SK, Rao SA, et al (2007) El Niño Modoki and its possible teleconnection. J
416 Geophys Res Ocean. doi: 10.1029/2006JC003798

417 Back LE, Bretherton CS (2009) On the relationship between SST gradients, boundary layer
418 winds, and convergence over the tropical oceans. J Climate 22: 4182–4196. doi:
419 10.1175/2009JCLI2392.1

420 Battisti DS, Sarachik ES, Hirst AC (1999) A consistent model for the large-scale steady surface
421 atmospheric circulation in the tropics. J Climate 12: 2956–2964. doi: 10.1175/1520-
422 0442(1999)012<2956:ACMFTL>2.0.CO;2

423 Bergman JW, Hendon HH (2000) Cloud radiative forcing of the low-latitude tropospheric
424 circulation: linear calculations. J Atmos Sci 57: 2225–2245. doi: 10.1175/1520-
425 0469(2000)057<2225:CRFOTL>2.0.CO;2

426 Bjerknes J (1969) Atmospheric teleconnections from the equatorial Pacific. Mon Weather Rev
427 97: 163–172. doi: 10.1175/1520-0493(1969)097<0163:ATFTEP>2.3.CO;2

428 Chiang JCH, Zebiak SE, Cane M a. (2001) Relative roles of elevated heating and surface
429 temperature gradients in driving anomalous surface winds over tropical oceans. J Atmos Sci
430 58: 1371–1394. doi: 10.1175/1520-0469(2001)058<1371:RROEHA>2.0.CO;2

Dee DP, Uppala S (2009) Variational bias correction of satellite radiance data in the ERA-Interim reanalysis. Q J R Meteorol Soc 135: 1830–1841. doi: 10.1002/qj.493

Dee DP, Uppala SM, Simmons AJ, et al (2011) The ERA-Interim reanalysis: configuration and performance of the data assimilation system. Q J R Meteorol Soc 137: 553–597. doi: 10.1002/qj.828

Bergman JW, Hendon HH (2000) Cloud radiative forcing of the low-latitude tropospheric circulation: linear calculations. J Atmos Sci 57: 2225–2245. doi: 10.1175/1520-0469(2000)057<2225:CRFOTL>2.0.CO;2

Deng Y, Park T-W, Cai M (2012) Process-based decomposition of the global surface temperature response to El Niño in boreal winter. J Atmos Sci 69: 1706–1712. doi: 10.1175/JAS-D-12-023.1

DeWeaver E, Nigam S (2004) On the forcing of ENSO teleconnections by anomalous heating and cooling. J Climate 17: 3225–3235. doi: 10.1175/1520-0442(2004)017<3225:OTFOET>2.0.CO;2

Fu Q, Liou KN (1992) On the correlated k-distribution method for radiative transfer in nonhomogeneous atmospheres. J Atmos Sci 49: 2139–2156.

Fu Q, Liou KN (1993) Parameterization of the radiative properties of cirrus clouds. J Atmos Sci 50: 2008–2025.

Gill AE (1980) Some simple solutions for heat induced tropical circulation. Q J R Meteorol Soc 106: 447–462.

451 Hoskins BJ, Karoly DJ (1981) The steady linear response of a spherical atmosphere to thermal
452 and orographic forcing. J Atmos Sci 38: 1179–1196.

453 Hsu HH (1994) Relationship between tropical heating and global girculation - interannual
454 variability. J Geophys Res 99: 10473–10489.

455 Hu X, Yang S, Cai M (2016) Contrasting the eastern Pacific El Niño and the central Pacific El
456 Niño: process-based feedback attribution. Climate Dyn 47: 2413–2424. doi:
457 10.1007/s00382-015-2971-9

458 Kao HY, Yu JY (2009) Contrasting Eastern-Pacific and Central-Pacific types of ENSO. J
459 Climate 22: 615–632. doi: 10.1175/2008JCLI2309.1

460 Larkin NK (2005) Global seasonal temperature and precipitation anomalies during El Niño
461 autumn and winter. Geophys Res Lett 32: L16705. doi: 10.1029/2005GL022860

462 Lee SK, Wang C, Mapes BE (2009) A simple atmospheric model of the local and teleconnection
463 responses to tropical heating anomalies. J Climate 22: 272–284. doi:
464 10.1175/2008JCLI2303.1

465 Lindzen RS, Nigam S (1987) On the role of sea surface temperature gradients in forcing low-
466 level winds and convergence in the Tropics. J Atmos Sci 44: 2418–2436. doi:
467 10.1175/1520-0469(1987)044<2418:OTROSS>2.0.CO;2

468 Lyon B, Barnston AG (2005) ENSO and the spatial extent of interannual precipitation extremes
469 in tropical land areas. J Climate 18: 5095–5109. doi: 10.1175/JCLI3598.1

470 Nguyen H, Evans A, Lucas C, et al (2013) The Hadley circulation in reanalyses: climatology,
471 variability, and change. J Climate 26: 3357–3376. doi: 10.1175/JCLI-D-12-00224.1

472 Oort AH, Yienger JJ (1996) Observed interannual variability in the Hadley circulation and its
473 connection to ENSO. J Climate 9: 2751–2767.

474 Philander SG (1990) El Niño, La Niña, and the Southern Oscillation. Academic Press, 293 pp.

475 Power SB, Smith IN (2007) Weakening of the Walker Circulation and apparent dominance of El
476 Niño both reach record levels, but has ENSO really changed? Geophys Res Lett 34:
477 L18702. doi: 10.1029/2007GL030854

478 Prabhakara C, Short DA, Vollmer BE (1985) El Niño and atmospheric water vapor: observations
479 from Nimbus 7 SMMR. J Clim Appl Meteorol 24: 1311–1324.

480 Rasmusson EM, Carpenter TH (1982) Variations in tropical sea surface temperature and surface
481 wind fields associated with the Southern Oscillation/El Niño. Mon Weather Rev 110: 354–
482 384.

483 Rasmusson EM, Kingtse Mo (1993) Linkages between 200-mb tropical and extratropical
484 circulation anomalies during the 1986-1989 ENSO cycle. J Climate 6: 595–616.

485 Rasmusson EM, Wallace JM (1983) Meteorological sspects of the El Niño/Southern Oscillation.
486 Science 222: 1195–1202. doi: 10.1126/science.222.4629.1195

487 Scherllin-Pirscher B, Steiner AK, Kirchengast G, et al (2011) Empirical analysis and modeling
488 of errors of atmospheric profiles from GPS radio occultation. Atmos Meas Tech 4: 1875–
489 1890. doi: 10.5194/amt-4-1875-2011

490 Sejas SA, Cai M, Liu G, et al (2016) A Lagrangian view of longwave radiative fluxes for
491 understanding the direct heating response to a CO2 increase. J Geophys Res Atmos 121:
492 6191–6214. doi: 10.1002/2015JD024738

493 Sun Y, Zhou TJ, Zhang LX (2013) Observational analysis and numerical simulation of the
494 interannual variability of the boreal winter Hadley circulation over the recent 30 years. Sci
495 China Earth Sci 56: 647–661. doi: 10.1007/s11430-012-4497-x

496 Takahashi H, Su H, Jiang JH, et al (2013) Tropical water vapor variations during the 2006-2007
497 and 2009-2010 El Niños: satellite observation and GFDL AM2.1 simulation. J Geophys Res
498 Atmos 118: 8910–8920. doi: 10.1002/jgrd.50684

499 Trenberth KE, Branstator GW, Karoly D, et al (1998) Progress during TOGA in understanding
500 and modeling global teleconnections associated with tropical sea surface temperatures. J
501 Geophys Res 103: 14291–14324. doi: 10.1029/97jc01444

502 Wang B, Wu R, Fu X (2000) Pacific–East Asian teleconnection: how does ENSO affect East
503 Asian climate? J Climate 13: 1517–1536. doi: 10.1175/1520-
504 0442(2000)013<1517:PEATHD>2.0.CO;2

505 Wang H, Kumar A, Wang W, Xue Y (2012) Influence of ENSO on Pacific decadal variability:
506 an analysis based on the NCEP climate forecast system. J Climate 25: 6136–6151. doi:
507 10.1175/JCLI-D-11-00573.1

508 Wang H, Su W (2013) Evaluating and understanding top of the atmosphere cloud radiative
509 effects in Intergovernmental Panel on Climate Change (IPCC) Fifth Assessment Report
510 (AR5) Coupled Model Intercomparison Project Phase 5 (CMIP5) models using satellite
511 observations. J Geophys Res Atmos 118: 683–699. doi: 10.1029/2012JD018619

512 White FM (2008) Pressure distribution in a fluid. Fluid Mechanics. New York: McGraw-Hill.
513 63–107 pp.

514 Wu Z (2003) A shallow CISK, deep equilibrium mechanism for the interaction between large-
515 scale convection and large-scale circulations in the tropics. J Atmos Sci 60: 377–392. doi:
516 10.1175/1520-0469(2003)060<0377:ASCDEM>2.0.CO;2

517 Wu Z, Sarachik ES, Battisti DS (2000) Vertical structure of convective heating and the three-
518 dimensional structure of the forced circulation on an equatorial beta plane. J Atmos Sci 57:
519 2169–2187. doi: 10.1175/1520-0469(2000)057<2169:VSOCHA>2.0.CO;2

520 Yuan Y, Yang S (2012) Impacts of different types of El Niño on the East Asian climate: focus on
521 ENSO cycles. J Climate 25: 7702–7722. doi: 10.1175/JCLI-D-11-00576.1

522 Zebiak SE (1986) Atmospheric convergence feedback in a simple model for El Niño. Mon
523 Weather Rev 114: 1263–1271.

524 Zhang X, Lin H, Jiang J (2012) Global response to tropical diabatic heating variability in boreal
525 winter. Adv Atmos Sci 29: 369–380. doi: 10.1007/s00376-011-1049-9

526 **Figures and Captions**

527 Figure 1. Composite DJF-mean anomalies in El Niño winters of observed (a) land and sea surface
528 temperature (SST) anomalies (K) and (b) upward longwave radiative flux anomalies ($W/m^2$).
529 Stippling indicates the 90% confidence level of statistical significance. Zonal means are
530 excluded.

531 Figure 2. Composite DJF-mean anomalies of observed geopotential height anomalies (in units of
532 m) at (a) 200 hPa, (b) 300 hPa, (c) 500 hPa, (d) 700 hPa, (e) 850 hPa, and (f) 950 hPa for El

Niño winters. Stippling indicates the 90% confidence level of statistical significance. Zonal means are excluded.

Figure 3. Same as Fig. 2 but for air temperature anomalies in units of K.

Figure 4. Composite DJF-mean anomalies of observed water vapor anomalies (in units of $kg/m^2$) in the layers of (a) 250-150 hPa, (b) 400-250 hPa, (c) 600-400 hPa, (d) 800-600 hPa, (e) 925-800 hPa, and (e) 1000-925 hPa for El Niño winters. Stippling indicates the 90% confidence level of statistical significance. Zonal means are excluded.

Figure 5. Same as Fig. 4 but for cloud water/ice content anomalies in units of $g/m^2$.

Figure 6. Composite DJF-mean anomalies of observed precipitation (in units of mm/day) for El Niño winters. Stippling indicates the 90% confidence level of statistical significance.

Figure 7. Same as Fig. 2 but for vertical velocity (ω) anomalies in units of Pa/s.

Figure 8. Air temperature-induced radiative cooling rate anomalies (in units ~~of~~ of $W/m^2$) in the layers of (a) 250-150 hPa, (b) 400-250 hPa, (c) 600-400 hPa, (d) 800-600 hPa, (e) 925-800 hPa, and (e) 1000-925 hPa.

Figure 9. Vertical profile of pattern-amplitude projection coefficients of the patterns in Figs. 10-13 onto the pattern shown in Fig. 8 (units $W/m^2$). Note that "Total" corresponds to

549 $\sqrt{A^{-1}\int_A a^2(\Delta^{(T_{air})}R_j)^2\cos\phi d\lambda d\phi}\sqrt{A^{-1}\int_A a^2(\Delta^{(T_{air})}Q_j)^2\cos\phi d\lambda d\phi}$ , the amplitude of $\Delta^{(T_{air})}R$

550 $\Delta^{(T_{air})}Q$ at the j[th] layer over domain A (90° E-90° W and 30° S-30° N).

551 Figure 10. Same as Fig. 8 but for the SST-induced radiative heating rate anomalies in units of

552 W/m$^2$.

553 Figure 11. Same as Fig. 8 but for the water vapor-induced radiative heating rate anomalies in units

554 of W/m$^2$.

555 Figure 12. Same as Fig. 8 but for the cloud-induced radiative heating rate anomalies in units of

556 W/m$^2$.

557 Figure 13. Same as Fig. 8 but for the non-radiative dynamic heating rate anomalies in units of

558 W/m$^2$.

559

Field Code Changed

Field Code Changed

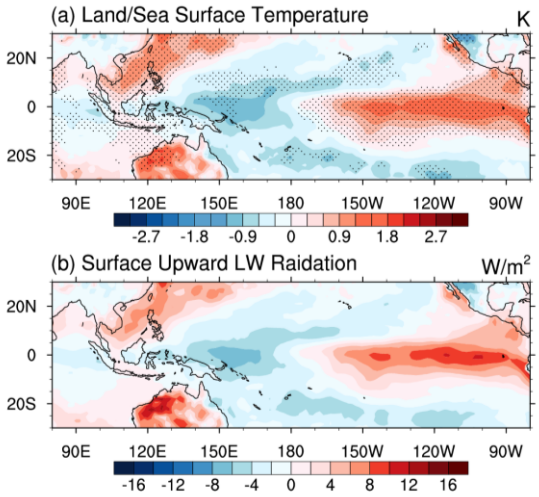


560

561 Figure 1. Composite DJF-mean anomalies in El Niño winters of observed (a) land and sea surface
562 temperature anomalies (K) and (b) upward longwave radiative flux anomalies ($W/m^2$).
563 Stippling indicates the 90% confidence level of statistical significance. Zonal means are
564 excluded.

565

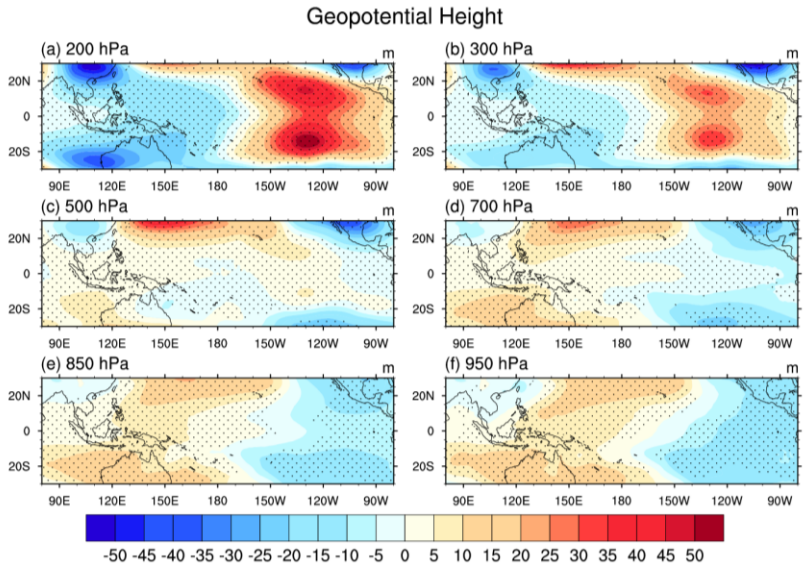


566

567 Figure 2. Composite DJF-mean anomalies of observed geopotential height anomalies (in units of
568 m) at (a) 200 hPa, (b) 300 hPa, (c) 500 hPa, (d) 700 hPa, (e) 850 hPa, and (f) 950 hPa for El
569 Niño winters. Stippling indicates the 90% confidence level of statistical significance. Zonal
570 means are excluded.

571

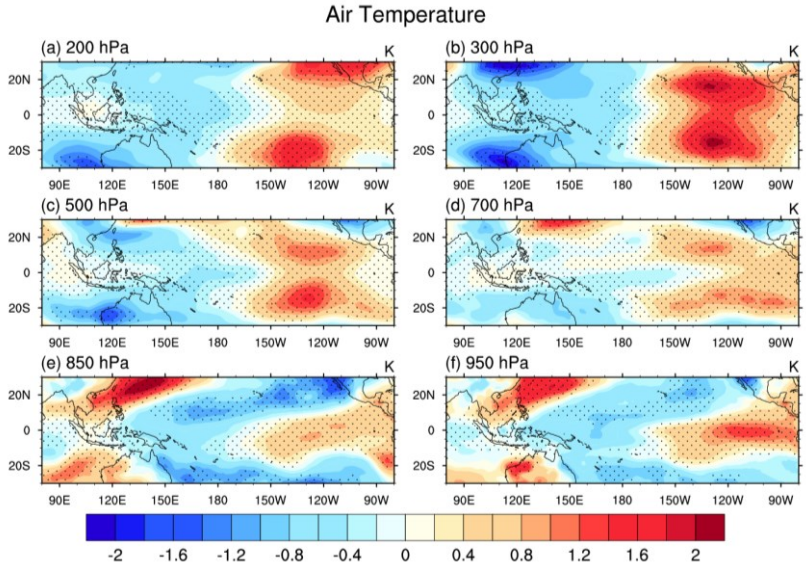


572

573 Figure 3. Same as Fig. 2 but for air temperature anomalies in units of K.

574

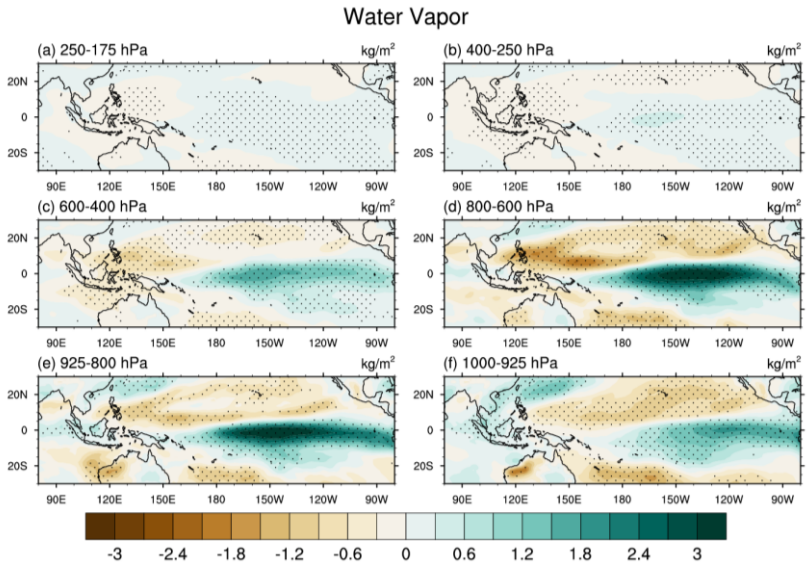


575

576 Figure 4. Composite DJF-mean anomalies of observed water vapor anomalies (in units of kg/m$^2$)
577 in the layers of (a) 250-150 hPa, (b) 400-250 hPa, (c) 600-400 hPa, (d) 800-600 hPa, (e) 925-
578 800 hPa, and (e) 1000-925 hPa for El Niño winters. Stippling indicates the 90% confidence
579 level of statistical significance. Zonal means are excluded.

580

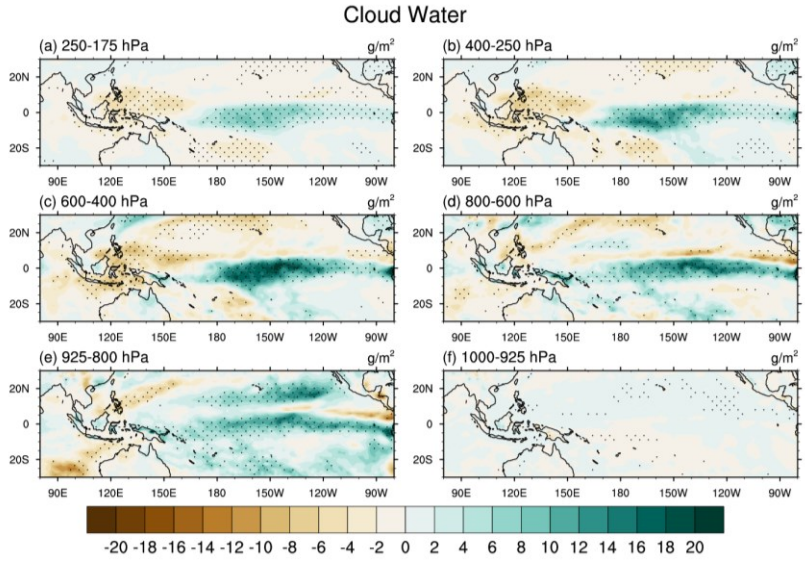


581

582 Figure 5. Same as Fig. 4 but for cloud water/ice content anomalies in units of g/m$^2$.

583

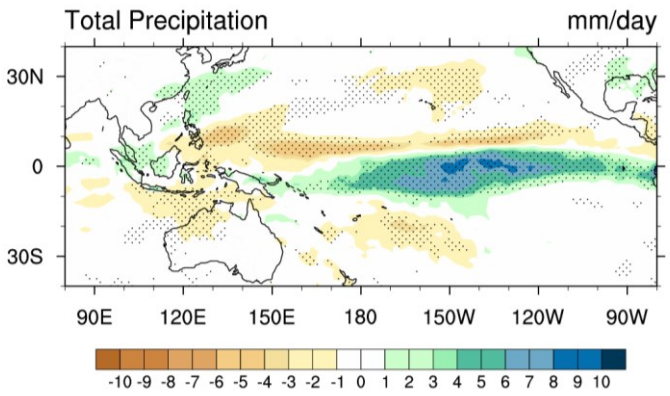


584

585 Figure 6. Composite DJF-mean anomalies of total precipitation (in units of mm/day) for El Niño

586 winters. Stippling indicates the 90% confidence level of statistical significance.

587

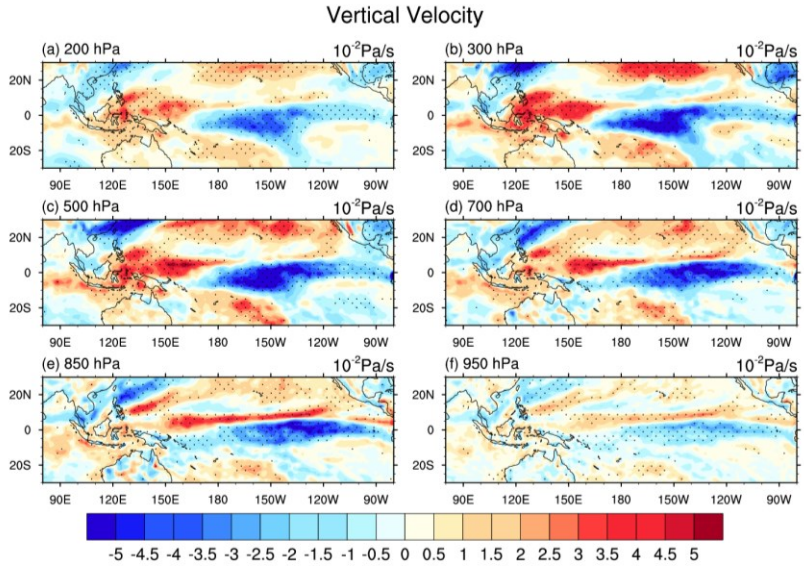


588

589 Figure 7. Same as Fig. 2 but for vertical velocity (ω) anomalies in units of Pa/s.

590

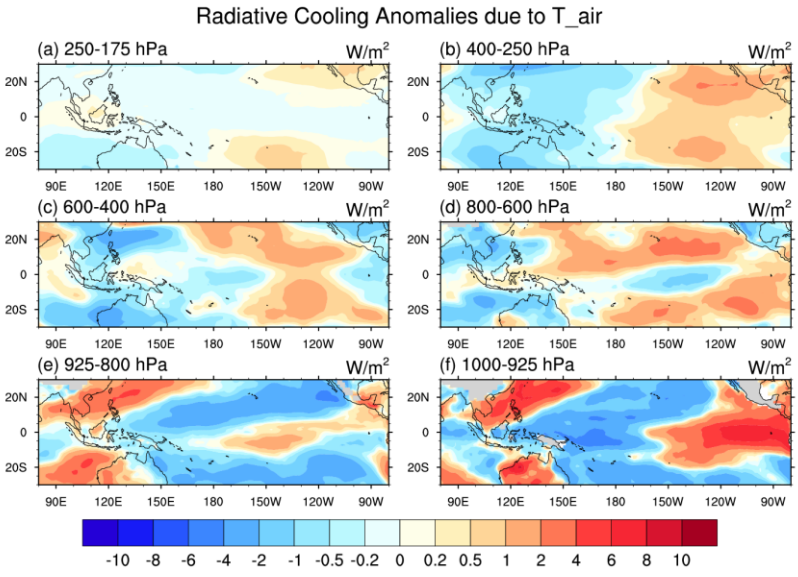


591

592 Figure 8. Air temperature-induced radiative cooling rate anomalies in units of W/m$^2$ in the layer

593 of (a) 250-150 hPa, (b) 400-250 hPa, (c) 600-400 hPa, (d) 800-600 hPa, (e) 925-800 hPa, and

594 (f) 1000-925 hPa.

595

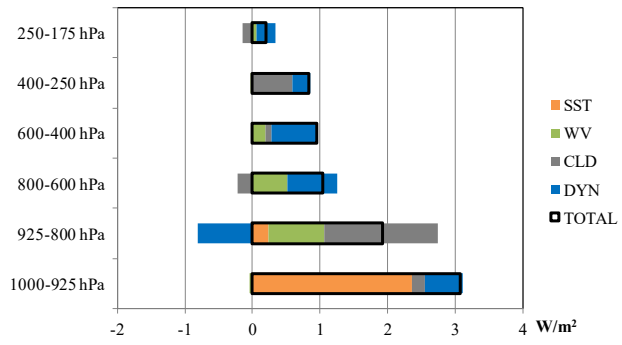


Figure 9. Vertical profile of pattern-amplitude projection coefficients of the patterns in Figs. 10-13 onto the pattern shown in Fig. 8 (units W/m$^2$). Note that "Total" corresponds to $\sqrt{A^{-1}\int_A a^2(\Delta^{(T_{air})}R_j)^2\cos\phi d\lambda d\phi}$, the amplitude of $\Delta^{(T_{air})}R$ at the j$^{th}$ layer over domain A (90° E-90° W and 30° S-30° N).

~~Figure 9. Vertical profile of pattern-amplitude projection coefficients of the patterns in Figs. 10-13 onto the pattern shown in Fig. 8 (units W/m$^2$). Note that "Total" corresponds to $\sqrt{A^{-1}\int_A a^2(\Delta^{(T_{air})}Q_j)^2\cos\phi d\lambda d\phi}$, the amplitude of $\Delta^{(T_{air})}Q$ at the j$^{th}$ layer over domain A (90° E-90° W and 30° S-30° N).~~

Field Code Changed

Field Code Changed

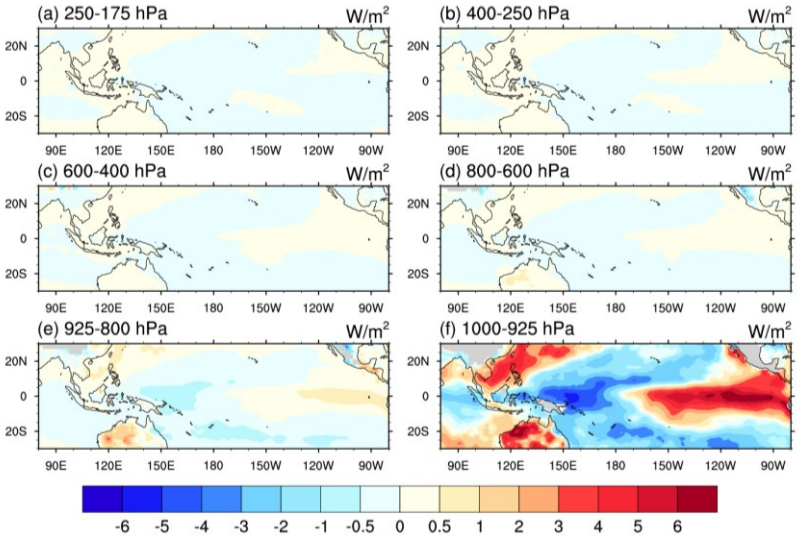


606

607 Figure 10. Same as Fig. 8 but for the SST-induced radiative heating rate anomalies in units of

608 $W/m^2$.

609

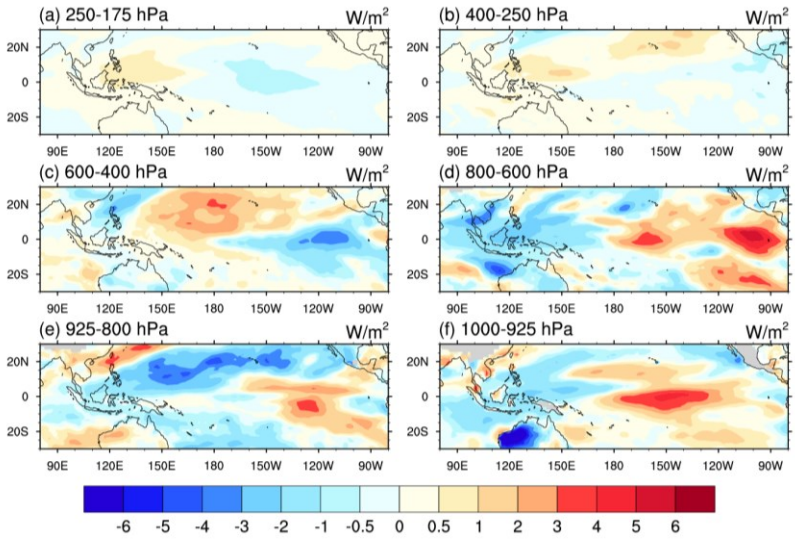


610

611 Figure 11. Same as Fig. 8 but for the water vapor-induced radiative heating rate anomalies in units

612 of W/m$^2$.

613

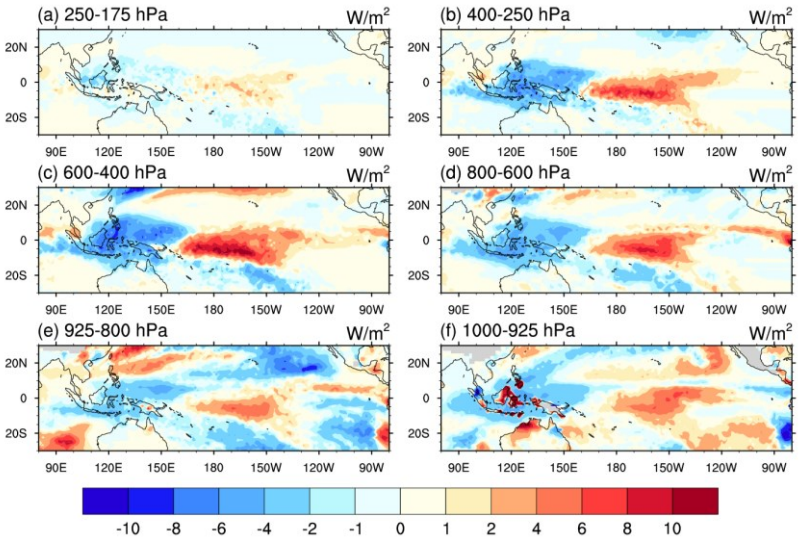


614

615 Figure 12. Same as Fig. 8 but for the cloud-induced radiative heating rate anomalies in units of

616 $W/m^2$.

617

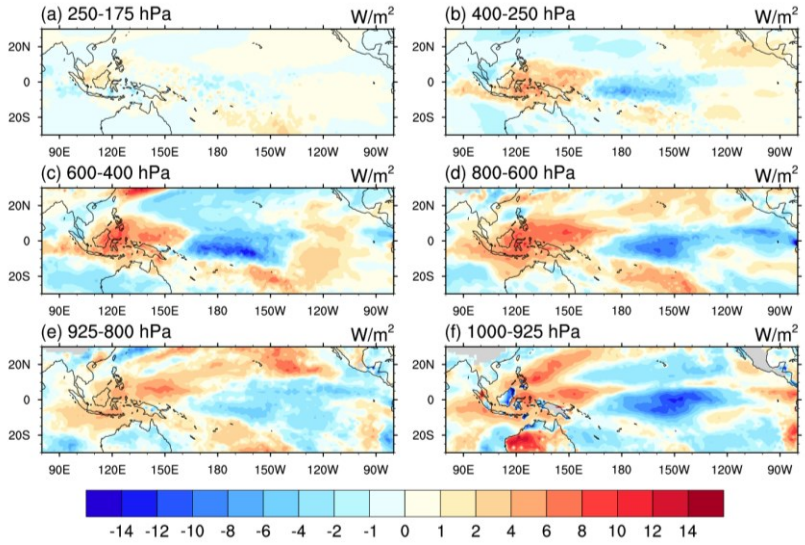


618

619 Figure 13. Same as Fig. 8 but for the non-radiative dynamic heating rate anomalies in units of

620 $W/m^2$.

621